JACS Au
AN OPEN ACCESS JOURNAL OF THE AMERICAN CHEMICAL SOCIETY

pubs.acs.org/jacsau

Letter

Spectroscopic Evidence for a Cobalt-Bound Peroxyhemiacetal Intermediate

Yeongjin Son, Kyungmin Kim, Seonghan Kim, Guilherme L. Tripodi, Aleksandr Pereverzev, Jana Roithová,* and Jaeheung Cho*

Cite This: *JACS Au* 2021, 1, 1594–1600

Read Online

ACCESS | Metrics & More | Article Recommendations | Supporting Information

ABSTRACT: Aldehyde deformylation reactions by metal dioxygen adducts have been proposed to involve peroxyhemiacetal species as key intermediates. However, direct evidence of such intermediates has not been obtained to date. We report the spectroscopic characterization of a mononuclear cobalt(III)-peroxyhemiacetal complex, $[Co(Me_3\text{-}TPADP)(O_2CH(O)CH(CH_3)C_6H_5)]^+$ (**2**), in the reaction of a cobalt(III)-peroxo complex (**1**) with 2-phenylpropionaldehyde (2-PPA). The formation of **2** is also investigated by isotope labeling experiments and kinetic studies. The conclusion that the peroxyhemiacetalcobalt(III) intermediate is responsible for the aldehyde deformylation is supported by the product analyses. Furthermore, isotopic labeling suggests that the reactivity of the cobalt(III)-peroxo complex depends on the second reactant. The aldehyde inserts between the oxygen atoms of **1**, whereas the reaction with acyl chlorides proceeds by a nucleophilic attack. The observation of the peroxyhemiacetal intermediate provides significant insight into the initial step of aldehyde deformylation by metalloenzymes.

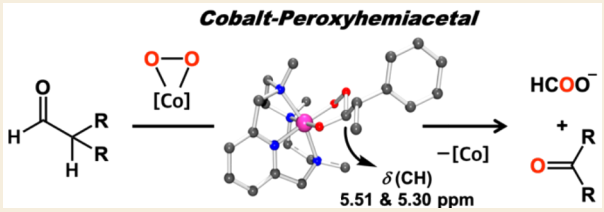

KEYWORDS: *bioinorganic chemistry, cobalt-dioxygen adduct, peroxyhemiacetal species, aldehyde deformylation, dichotomic reactivity*

The aldehyde deformylation reaction catalyzed by metalloenzymes plays a crucial role in the biosynthesis of many molecules and has potential applications in developing sustainable biofuels.[1−3] As a well-known example, cytochrome P-450 aromatase catalyzes the three oxidative steps for biotransformation of androgens to estrogens.[4−6] Among the steps, the deformylation process has been suggested to include the nucleophilic attack of a ferric peroxo species to the carbonyl carbon of androstenedione to form a putative peroxyhemiacetal adduct, producing the estrone.[7−10]

To understand the mechanism of aldehyde deformylation, numerous biomimetic heme/nonheme mononuclear metal-dioxygen adducts have been synthesized and investigated in substrate oxidation reactions.[11−22] Valentine and co-workers demonstrated that the ferric peroxo porphyrin species reacts with the substrate of aromatase, which was proposed to proceed through direct nucleophilic attack by the peroxo ligand (Scheme 1, NA pathway).[13] Since then, much research has been focused on controlling the nucleophilic reactivity on the basis of the peroxyhemiacetal proposal. The ring size of the supporting macrocyclic ligands has been shown to regulate the nucleophilic reactivity of the mononuclear side-on cobalt(III)-peroxo complexes.[14] The axial ligand effect has been highlighted in manganese(III)-peroxo complexes; it was suggested that the axial anionic ligand changed the MnO_2 core from a side-on to an end-on mode, resulting in a higher nucleophilic character on the peroxo moiety.[17] In addition, an alternative mechanism involving a hydrogen atom abstraction

Scheme 1. Proposed Pathways for Nucleophilic Attack (NA) vs Hydrogen Atom Abstract (HAA) in Aldehyde Deformylation

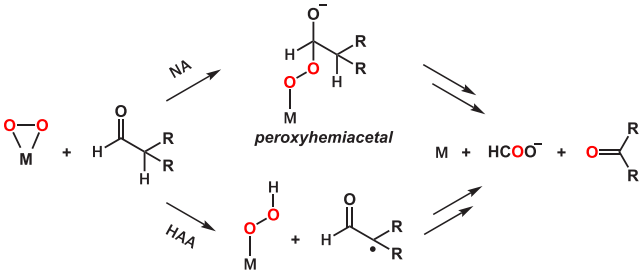

pathway has been reported recently, in which the α-hydrogen atom of aldehyde substrates was abstracted by manganese(III)-peroxo species with a kinetic isotope effect (Scheme 1, HAA pathway).[18−20] McDonald and co-workers reported the nucleophilic reactivity of a Cu(II)-superoxo complex, $[LCuO_2]^-$ (L = *N*,*N*-bis(2,6-diisopropylphenyl)-2,6-pyridinedicarboxamide), based on the peroxyhemiacetal route.[21]

Received: April 13, 2021
Published: October 6, 2021

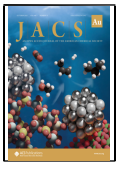

However, the very same complex reacted with 2-phenylpropionaldehyde (2-PPA) by deprotonating the benzylic position to form a copper(II)-enolate complex, [LCu(OC═(Me)Ph)]$^{-}$, suggesting the enolate pathway for the deformylation reaction.[22] Next to these mechanistic pathways lies an alternative pathway of the insertion of the carbonyl function between the oxygen atoms of the peroxo reactant in analogy with the reactivity proposed for nitrile and naphthalene activation.[23,24] Thus, there is still substantial debate on the initial step in the aldehyde deformylation. Although the peroxyhemiacetal pathway has been well accepted over the past several decades, the reactive intermediates have not yet been observed and characterized in biological and model systems.

Herein, we report the isolation of a peroxyhemiacetal intermediate in the reaction of a Co(III)-peroxo complex, [Co(Me$_3$-TPADP)(O$_2$)]$^{+}$ (**1**; Me$_3$-TPADP = 3,6,9-trimethyl-3,6,9-triaza-1(2,6)-pyridinacyclodecaphane), and 2-PPA. The Co(III)-peroxyhemiacetal complex [Co(Me$_3$-TPADP)(O$_2$CH(O)CH(CH$_3$)C$_6$H$_5$)]$^{+}$ (**2**) has been characterized by various physicochemical methods such as UV−vis, CSI-MS, and ^{1}H NMR. Kinetic studies and isotope labeling experiments support the formation of **2**, and the thermal decomposition of **2** clearly shows deformylated products. Such peroxyhemiacetal chemistry has been extended to other aldehydes; the reaction of **1** and the aldehydes produces the corresponding peroxyhemiacetal intermediates, which are active for the aldehyde deformylation as well.

The Co(III)-peroxo complex **1** was prepared by the addition of H$_2$O$_2$ and triethylamine (TEA) into a CH$_3$CN solution of a Co(II) complex, [Co(Me$_3$-TPADP)(CH$_3$CN)$_2$]$^{2+}$, as previously reported.[25] Single crystals of **1**-ClO$_4$·CH$_3$CN were grown by diffusion of diethyl ether into a CH$_3$CN solution of **1** at −40 °C (see Tables S1 and S2 in the Supporting Information for crystallographic data for **1**). The X-ray crystal structure of **1** clearly revealed the mononuclear side-on cobalt-peroxo core in a distorted-octahedral geometry (Figure 1a). The O−O bond

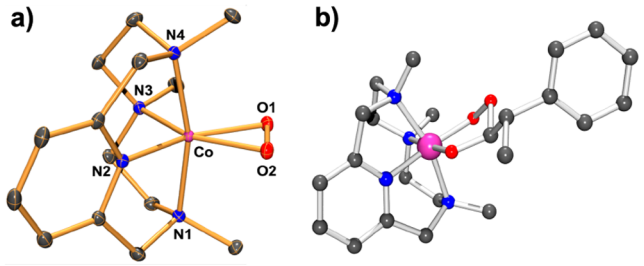

Figure 1. Structures of complexes. Hydrogen atoms are omitted for clarity. (a) ORTEP diagram of **1** with thermal ellipsoids drawn at the 30% probability level. (b) DFT-optimized structure of **2**. Color code: pink, Co; red, O; blue, N; gray, C.

length of 1.4611(19) Å is characteristic of a peroxide ligand, as supported by the resonance Raman data (ν(O−O) = 888 cm^{-1}).[25] The O−O vibrational frequency of **1** was further confirmed using helium-tagging infrared photodissociation (IRPD) spectroscopy.[26,27] The IRPD spectrum of **1** showed an isotope-sensitive band at 921 cm^{-1} that shifted to 869 cm^{-1} when H$_2$^{18}O$_2$ was used (Figure 2a and Figure S2). The isotopic shift is fully in agreement with the shift expected on the basis of Hooke's law.

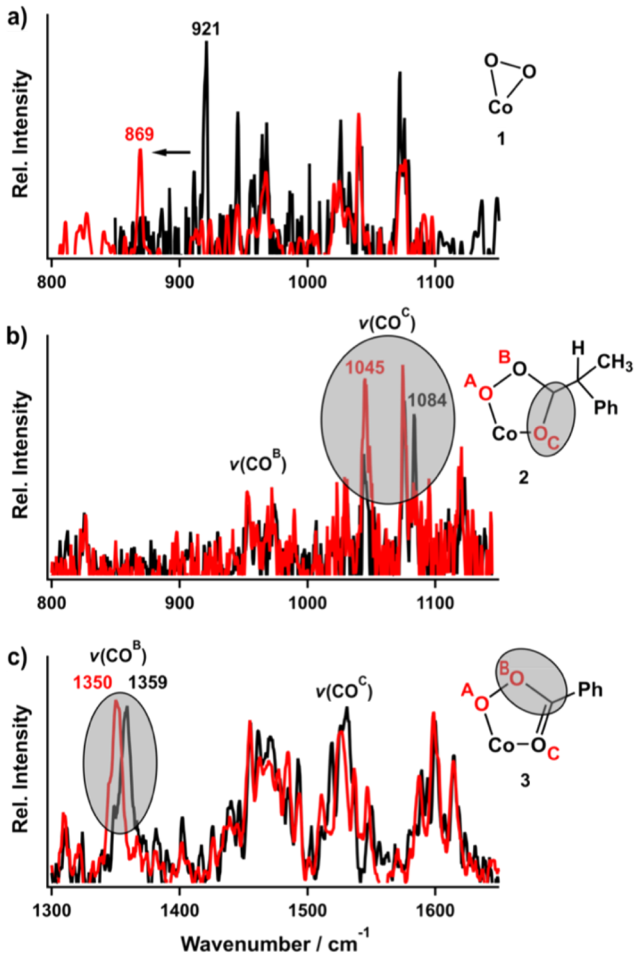

Figure 2. Helium tagging infrared photodissociation spectra of mass-selected (a) **1**-^{16}O (m/z 339, black line) and **1**-^{18}O (m/z 443, red line), (b) **2**-^{16}O (m/z 473, black line) and **2**-^{18}O (m/z 477, red line), and (c) **3**-^{16}O (m/z 222, black line) and **3**-^{18}O (m/z 224, red line). See Figures S2, S3, and S29 for further details.

Complex **2** was generated by adding excess amounts of 2-PPA to a solution of **1**. Upon addition of 2-PPA to **1** in CH$_3$CN at 0 °C, the solution turned from blue to green, where the absorption bands of **2** increased at 400 (ε = 616 M^{-1} cm^{-1}) and 680 nm (ε = 174 M^{-1} cm^{-1}) (Figure 3a). Cold spray ionization mass spectrometry (CSI-MS) of the green solution of **2** suggested the formation of the 2-PPA adduct of **1** with a signal at a mass to charge ratio (m/z) of 473.3, [Co(Me$_3$-TPADP)(O$_2$CH(O)CH(CH$_3$)C$_6$H$_5$)]$^{+}$ (**2**-^{16}O) (calculated m/z 473.2) (Figure 3b), together with **1** due to an equilibrium between **1** and **2** (*vide infra*). When the reaction was performed with isotopically labeled [Co(Me$_3$-TPADP)(^{18}O$_2$)]$^{+}$ (**1**-^{18}O), a mass peak corresponding to [Co(Me$_3$-TPADP)(^{18}O$_2$CH(O)CH(CH$_3$)C$_6$H$_5$)]$^{+}$ (**2**-^{18}O) appeared at m/z 477.3 (calculated m/z 477.2) (Figure S4). The observation of the shift of 4 mass units indicated that **2** contains an O$_2$ unit. Collision-induced dissociation of mass-selected **2** leads to the elimination of 2-PPA and re-formation of **1** (Figure S1).

Helium tagging IRPD spectra of mass-selected **2**-^{16}O and **2**-^{18}O revealed an isotopically sensitive band at 1084 cm^{-1} that shifts upon ^{18}O labeling to 1045 cm^{-1} (Figure 2b). A comparison with DFT calculations suggests that this band

https://doi.org/10.1021/jacsau.1c00166
JACS Au 2021, 1, 1594−1600

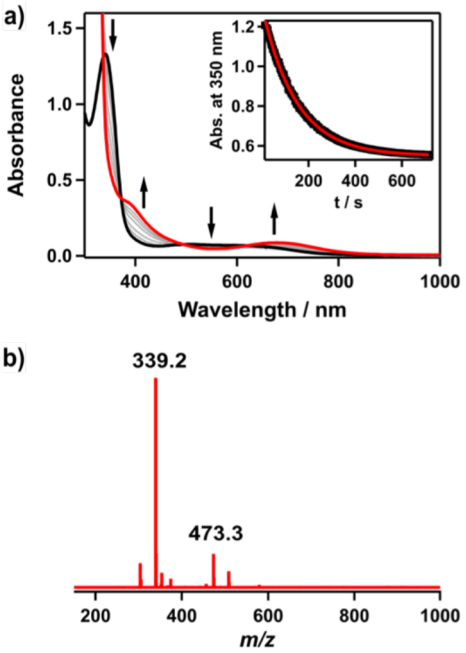

Figure 3. (a) UV−vis spectral changes observed in the reaction of **1** (0.5 mM) with 2-PPA (0.1 M) in CH_3CN at 0 °C. The inset shows the time course of the absorbance at 350 nm and its first-order fitting (red line). (b) CSI-MS spectrum of the reaction solution obtained in the reaction of **1** (0.5 mM) with 2-PPA (0.1 M). The peaks at *m*/*z* 339.2 and 473.3 are assigned to $[Co(Me_3\text{-TPADP})(O)_2]^+$ (**1**) and $[Co(Me_3\text{-TPADP})(O_2CH(O)CH(CH_3)C_6H_5)]^+$ (**2**), respectively.

corresponds to the C−O(Co) stretching vibration of the peroxyhemiacetal complex, consistent with a carbonyl insertion between the oxygen atoms of **1** (Figure S3). These results are similar to the carbonyl insertion of a bis(triphenylphosphine)-platinum-oxygen complex.[28] The O−O vibration is predicted to be at 870 cm^{-1} with extremely small intensity. Hence, it cannot be detected with the available instrumentation.

The ^1H NMR spectrum of **2** in acetonitrile-d_3 at −40 °C showed complicated signals because **2** is in equilibrium with **1** and 2-PPA (*vide infra*). By comparison with the NMR spectra of **1** and 2-PPA (Figures S5−S7), the characteristic peaks of **2** were distinguished and assigned by ^1H NMR, ^{13}C NMR, $^1H-^{13}C$ heteronuclear single quantum coherence (HSQC), and $^1H-^1H$ homonuclear correlation spectroscopy (COSY) (Figure 4b and Figures S8−S11). Interestingly, single C−H resonances associated with the peroxyhemiacetal moiety in **2** were observed in $^1H-^{13}C$ HSQC, where ^1H signals at 5.51 and 5.30 ppm are correlated with ^{13}C chemical shifts at 107.88 and 108.91 ppm, respectively, due to the formation of diastereomers by the two possible insertion sides of the carbonyl carbon of 2-PPA. The X-band EPR silence (Figure S12) and the NMR spectral features clearly indicate that **2** is a low-spin $S = 0$ peroxyhemiacetalcobalt(III) complex.

Density functional theory calculations were carried out as implemented in the Gaussian 09 computational package. Geometry optimization and frequency calculations for **1** and **2** were performed with the unrestricted B3LYP/6-31g* theory level for all atoms. The calculated O−O bond distance of **1** (1.441 Å) is similar to that of the crystal structure of **1** (1.461 Å) (Table S3). The electronic structures of intermediate **2** are described as a peroxyhemiacetalcobalt(III) complex form that has three possible energetically stable spin states ($S = 0, 1, 2$).

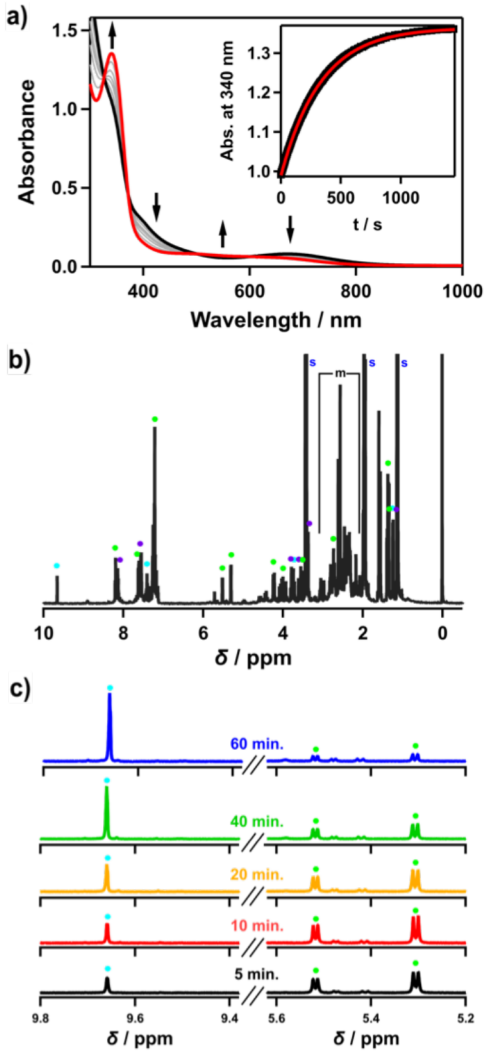

Figure 4. (a) UV−vis spectral change during the incubation of **2** (black line) in CH_3CN at 0 °C, affording **1** (red line). The inset shows the time course of the absorbance at 340 nm and its first-order fitting (red line). (b) ^1H NMR spectrum of the isolated **2** (8 mM) in CD_3CN at −40 °C (purple circles, **1**; green circles, **2**; cyan circles, 2-PPA). The multiplet signals (m) in the region at 2.0−3.0 ppm were derived from the NCH_2CH_2 moiety in **1** and **2**. (c) Time-dependent ^1H NMR spectra of incubation of the isolated **2** (8 mM) in CD_3CN at 0 °C.

The low-spin state of **2** showed the lowest energy in the calculations (Figure 1b and Tables S4−S6), which corresponds with the spectroscopic results. The O−O bond length of **2** is calculated to be 1.463 Å (Figure 1b), which is comparable to those of the acylperoxonickel(II) complex of the Hikichi group (1.443 Å).[29]

To understand the formation process of **2**, we performed kinetic studies of **1** with an excess amount of 2-PPA. During the reaction, the absorption band at 340 nm due to **1** disappeared, obeying first-order kinetics. The pseudo-first-order rate constant increased proportionally with an increase of 2-PPA concentration, giving a second-order rate constant of $3.4(2) \times 10^{-2}$ M^{-1} s^{-1}. The temperature dependence of the reaction rates was examined in the range of 253−283 K. A linear Eyring plot was obtained with activation parameters of $\Delta H^{\ddagger} = 11(1)$ kcal mol^{-1} and $\Delta S^{\ddagger} = -23(2)$ cal mol^{-1} K^{-1}

https://doi.org/10.1021/jacsau.1c00166
JACS Au 2021, 1, 1594−1600

Scheme 2. Equilibrium between 1 and 2

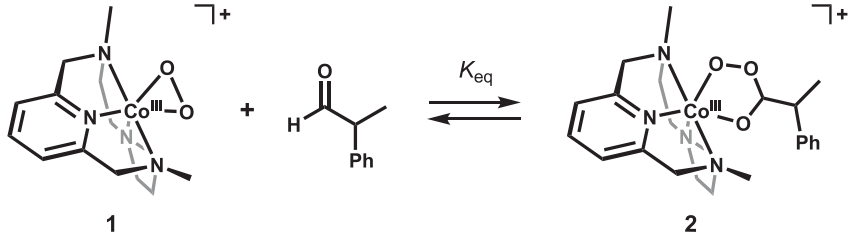

(Figure S13). The observed negative entropy value and the second-order kinetics suggest that the formation of **2** occurs via a bimolecular mechanism.

Upon incubation of the isolated sample of **2** (0.5 mM), which does not contain extra 2-PPA in CH_3CN at 0 °C, the intermediate readily reverted back to **1**, whose characteristic absorption bands were regenerated with isosbestic points at 326, 372, 501, and 600 nm (Figure 4a). The observed spectral change indicates the release of 2-PPA from **2**, which is found to be in equilibrium with **1** (Scheme 2). The equilibrium was further confirmed by using ^{1}H NMR measurements, where the characteristic single peroxyhemiacetal C−H resonances at 5.51 and 5.30 ppm disappear with the concomitant appearance of the aldehyde resonance at 9.65 ppm corresponding to 2-PPA (Figure 4c). A product analysis of the solution showed that 2-PPA was recovered intact. The equilibrium constant (K_{eq}) from optical titrations was determined to be 288 M^{-1} at 273 K (Figure S14).[30,31] These results demonstrated that the equilibrium lies to the left (Scheme 2).[32,33] The addition of an excess amount of 2-PPA shifts the equilibrium between **1** and **2** to the **2** side. The UV−vis spectrum of **2** could be obtained in the presence of a large excess of 2-PPA while the resulting green solution was maintained at 0 °C. The solution turned purple upon heating to 70 °C. The observed rate constant (k_{obs} = 2.0(1) × 10^{-3} s^{-1}) for the thermal decomposition with excess 2-PPA was independent of the 2-PPA concentration and led predominantly to the formation of acetophenone (83(3)%) as a deformylation product. After completion of the reaction, the ESI-MS spectrum revealed the formation of a Co(II)-formato complex together with the starting Co(II) species (Figures S15 and S16).

Then, we expanded the scope of substrates to cyclohexanecarboxaldehyde (CCA) and pivalaldehyde. **1** reacts with both CCA and pivalaldehyde in CH_3CN at 0 °C, affording the corresponding Co(III)-peroxyhemiacetal complexes, which were confirmed by UV−vis, ESI-MS, and ^{1}H NMR (Figures S17−S24). The k_2 values for the formation of Co(III)-peroxyhemiacetal adducts were determined to be 2.7(1) × 10^{-2} M^{-1} s^{-1} for CCA and 2.8(1) × 10^{-2} M^{-1} s^{-1} for pivalaldehyde (Figure S25). The thermal decomposition of the Co(III)-peroxyhemiacetal complexes in the presence of additional substrates was also examined at 70 °C. Product analyses of the final solution show oxidized organic products (Table S7 in the Supporting Information). These results suggest that the formation of the peroxyhemiacetal intermediate occurs in the oxidation of aldehydes as well as in aldehyde deformylation by **1**.

We have further explored the nucleophilic type of reactivity of **1** in a reaction with benzoyl chloride (Scheme 3a). The peroxide ligand simply displaces the chloride, which is a good leaving group, and the subsequent hydrolysis yields benzoic acid quantitatively, as determined by a product analysis of the final reaction mixture by GC-MS. UV−vis and ESI-MS show that the reaction is irreversible (no equilibrium; Figures S27 and S28).

Scheme 3. Proposed Mechanisms for Nucleophilic Attack (NA) vs O−O Insertion in Reactions of Co(III)-Peroxo Species

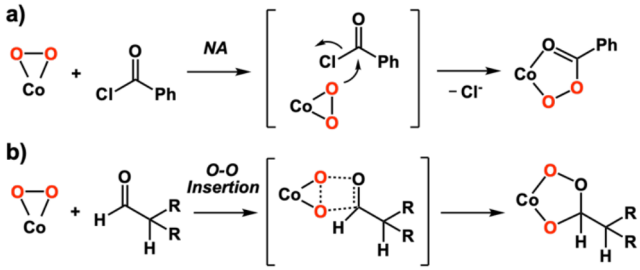

The Co(III)-perbenzoato intermediate [Co(Me_3-TPADP)-($O_2C(O)C_6H_5$)]$^{2+}$ (**3**) has been detected by CSI-MS (Figure S26). The structure was characterized by the IRPD spectrum of **3** (Figure 2c). In agreement with the nucleophilic pathway scenario (Scheme 3a and Scheme S1), the ^{18}O labeling of **1** results in a band shift of the C−O(O) vibration of **3** (note the difference between **3** and **2**). We have further modified the electrophilicity of the benzoyl chloride reactants by electron-withdrawing and -donating substituents at the *para* position of the phenyl group, *p*-X-PhC(O)Cl (X = Me, F, H, Cl, Br) (Figure 5a). The Hammett plot shows a ρ value of 3.2(1) (Figure 5b), fully consistent with the nucleophilic reaction pathway of the peroxo group of **1** in this reaction.

Our results show that cobalt(III)-peroxo complexes can have dichotomic reactivity; they can either insert between the oxygen atoms or react as nucleophiles. In order to understand these pathways, we have performed exploratory calculations using acetaldehyde as a model. Species **1** converts to Co(III)-dioxyl with a barrier of 31.1 kcal mol^{-1} (Figure 6a). Aldehyde insertion occurs with the C−O bond forming prior to the O−O bond. The reaction pathway leads across the singlet, triplet, and quintet potential energy surfaces, suggesting a strong multireference character of this reaction. Alternatively, coordination of the acetaldehyde to **1** can induce the formation of a cobalt(II)-superoxo complex via an energy barrier of 18.6 kcal mol^{-1} associated with a spin flip from the singlet to the triplet state (Figure 6b). The subsequent addition of the superoxo unit to the aldehyde carbonyl proceeds with a low energy barrier and a spin flip to the singlet state cobalt(III)-peroxyhemiacetal product.

Our spectroscopic data unambiguously show the insertion of 2-PPA into the O−O bond, which is the energy-disfavored pathway according to the DFT calculations. This discrepancy is most likely associated with the inaccuracy of DFT for energy and structure predictions for multireference systems. In

https://doi.org/10.1021/jacsau.1c00166
JACS Au 2021, 1, 1594−1600

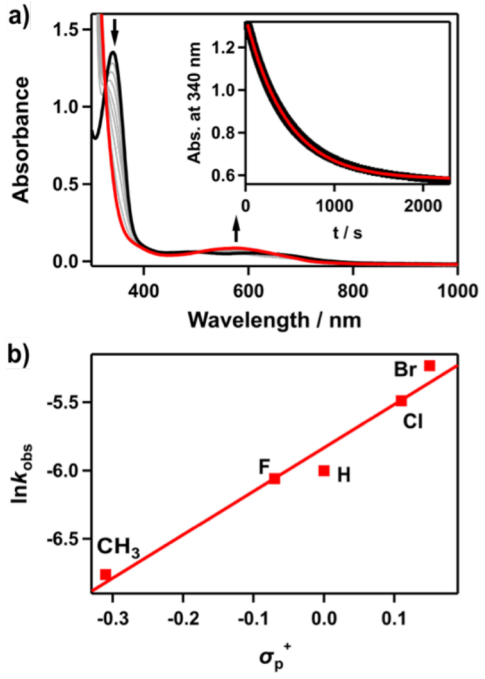

Figure 5. Reaction of **1** with acyl chlorides in CH_3CN at 0 °C. (a) UV−vis spectral changes of **1** (black line) upon addition of 50 equiv of benzoyl chloride. The inset shows the time course of the absorbance at 340 nm and its first-order fitting (red line). (b) Hammett plot of ln k_{obs} against σ_p^+ of *para*-substituted benzoyl chlorides, *p*-X-PhCOCl (X = CH_3, F, H, Cl, Br).

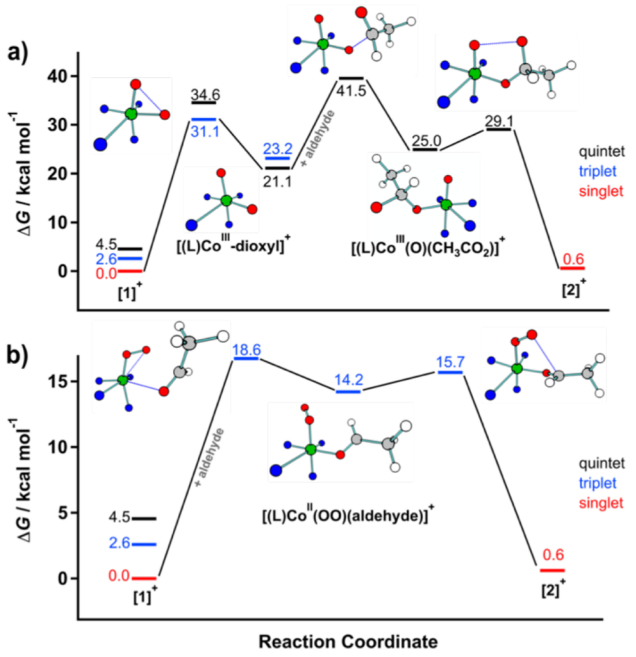

Figure 6. PES for the insertion (a) and nucleophilic addition (b) reaction pathways calculated at the B3LYP-D3/6-31+G* level of theory with the SMD model to account for acetonitrile solvation. The bonds being broken/formed at the transition states are represented in blue. The color codes are blue for nitrogen, gray for carbon, white for hydrogen, red for oxygen, and green for cobalt.

addition, the alternative [2 + 2] pathway suggested for the insertion mechanism (see Scheme 3b) could have not been localized at all at the DFT level. Again, the significant role of the multireference electronic structure of the probable transition structure could be a key in understanding the observed reactivity.[34−37]

In conclusion, we have shown that **2** is the first example of an isolable cobalt(III)-peroxyhemiacetal intermediate in aldehyde deformylation. Complex **2** has been trapped in the reaction of cobalt(III)-peroxo complex **1** with 2-PPA and was characterized by spectroscopic and spectrometric methods. Labeling experiments reveal that 2-PPA inserts between the oxygen atoms of the peroxo moiety in **1**. Species **1** and **2** are in equilibrium in solution, with a small equilibrium constant. In the presence of excess 2-PPA, **2** readily decomposed to cobalt(II) species and deformylated products. The formation of a peroxyhemiacetal species for the reaction of **1** with other aldehyde substrates was also observed. The nucleophilic addition pathway prevails for the reaction of **1** with acyl chlorides, and it is supported by the positive ρ value in the Hammett plot using *para*-substituted acyl chlorides. The present work provides spectroscopic evidence for and deeper insight into the metal-bound peroxyhemiacetal species invoked in the mechanisms for aldehyde deformylase and related biomimetic reactions.

■ ASSOCIATED CONTENT

Supporting Information

The Supporting Information is available free of charge at https://pubs.acs.org/doi/10.1021/jacsau.1c00166.

Experimental details for the generation and characterization of **2**, UV−vis, CSI-MS, and NMR data (^{1}H, ^{13}C, ^{1}H−^{1}H COSY, ^{1}H−^{13}C HSQC), generation and characterization of **3**, UV−vis, CSI-MS, IRPD spectra and DFT studies of **1**−**3**. plot of equilibrium constants between **1** and **2**, incubation experiments of **2** and **3**, product analysis by gas chromatography, and additional figures and tables as described in the text (PDF)

Crystallographic data for [Co(Me$_3$-TPADP)(O$_2$)](ClO$_4$)(MeCN) (CIF)

■ AUTHOR INFORMATION

Corresponding Authors

Jana Roithová − *Department of Spectroscopy and Catalysis, Institute for Molecules and Materials, Radboud University, 6525 AJ Nijmegen, The Netherlands*; Email: J.Roithova@science.ru.nl

Jaeheung Cho − *Department of Chemistry, Ulsan National Institute of Science and Technology (UNIST), Ulsan 44919, Korea*; orcid.org/0000-0002-2712-4295; Email: jaeheung@unist.ac.kr

Authors

Yeongjin Son − *Department of Chemistry, Ulsan National Institute of Science and Technology (UNIST), Ulsan 44919, Korea; Department of Emerging Materials Science, Daegu Gyeongbuk Institute of Science and Technology (DGIST), Daegu 42988, Korea*

Kyungmin Kim − *Department of Chemistry, Ulsan National Institute of Science and Technology (UNIST), Ulsan 44919, Korea; Department of Emerging Materials Science, Daegu Gyeongbuk Institute of Science and Technology (DGIST), Daegu 42988, Korea*; orcid.org/0000-0002-3362-128X

Seonghan Kim − *Department of Chemistry, Ulsan National Institute of Science and Technology (UNIST), Ulsan 44919,*

https://doi.org/10.1021/jacsau.1c00166
JACS Au 2021, 1, 1594−1600

Korea; Department of Emerging Materials Science, Daegu Gyeongbuk Institute of Science and Technology (DGIST), Daegu 42988, Korea

Guilherme L. Tripodi − *Department of Spectroscopy and Catalysis, Institute for Molecules and Materials, Radboud University, 6525 AJ Nijmegen, The Netherlands*

Aleksandr Pereverzev − *Department of Spectroscopy and Catalysis, Institute for Molecules and Materials, Radboud University, 6525 AJ Nijmegen, The Netherlands;* orcid.org/0000-0001-5486-6916

Complete contact information is available at: https://pubs.acs.org/10.1021/jacsau.1c00166

Notes

The authors declare no competing financial interest.

■ ACKNOWLEDGMENTS

The research was supported by National Research Foundation funded by the Ministry of Science, ICT and Future Planning of Korea (2019R1A2C2086249).

■ REFERENCES

(1) Dennis, M.; Kolattukudy, P. E. A Cobalt-Porphyrin Enzyme Converts a Fatty Aldehyde to a Hydrocarbon and CO. *Proc. Natl. Acad. Sci. U. S. A.* **1992**, *89*, 5306−5310.

(2) Schirmer, A.; Rude, M. A.; Li, X.; Popova, E.; del Cardayre, S. B. Microbial Biosynthesis of Alkanes. *Science* **2010**, *329*, 559−562.

(3) Warui, D. M.; Li, N.; Norgaard, H.; Krebs, C.; Bollinger, J. M.; Booker, S. J. Detection of Formate, Rather than Carbon Monoxide, As the Stoichiometric Coproduct in Conversion of Fatty Aldehydes to Alkanes by a Cyanobacterial Aldehyde Decarbonylase. *J. Am. Chem. Soc.* **2011**, *133*, 3316−3319.

(4) Thompson, E. A.; Siiteri, P. K. Utilization of Oxygen and Reduced Nicotinamide Adenine Dinucleotide Phosphate by Human Placental Microsomes during Aromatization of Androstenedione. *J. Biol. Chem.* **1974**, *249*, 5364−5372.

(5) Thompson, E. A.; Siiteri, P. K. The Involvement of Human Placental Microsomal Cytochrome P-450 in Aromatization. *J. Biol. Chem.* **1974**, *249*, 5373−5378.

(6) Korzekwa, K. R.; Trager, W. F.; Mancewicz, J.; Osawa, Y. Studies on the Mechanism of Aromatase and Other Cytochrome P450 Mediated Deformylation Reactions. *J. Steroid Biochem. Mol. Biol.* **1993**, *44*, 367−373.

(7) Stevenson, D. E.; Wright, J. N.; Akhtar, M. Mechanistic Consideration of P-450 Dependent Enzymic Reactions: Studies on Oestriol Biosynthesis. *J. Chem. Soc., Perkin Trans. 1* **1988**, 2043−2052.

(8) Watanabe, Y.; Ishimura, Y. Aromatization of Tetralone Derivatives by Fe^{III}PFP(Cl)/PhIO and Cytochrome P-450*cam*: A Model Study on Aromatase Cytochrome P-450 Reaction. *J. Am. Chem. Soc.* **1989**, *111*, 410−411.

(9) Watanabe, Y.; Ishimura, Y. A Model Study on Aromatase Cytochrome P-450 Reaction: Transformation of Androstene-3,17,19-trione to 10*β*-Hydroxyestr-4-ene-3,17-dione. *J. Am. Chem. Soc.* **1989**, *111*, 8047−8049.

(10) Cole, P. A.; Bean, J. M.; Robinson, C. H. Conversion of a 3-Desoxysteroid to 3-Desoxyestrogen by Human Placental Aromatase. *Proc. Natl. Acad. Sci. U. S. A.* **1990**, *87*, 2999−3003.

(11) Park, M. J.; Lee, J.; Suh, Y.; Kim, J.; Nam, W. Reactivities of Mononuclear Non-Heme Iron Intermediates Including Evidence that Iron(III)−Hydroperoxo Species Is a Sluggish Oxidant. *J. Am. Chem. Soc.* **2006**, *128*, 2630−2634.

(12) Goto, Y.; Wada, S.; Morishima, I.; Watanabe, Y. Reactivity of Peroxoiron(III) Porphyrin Complexes: Models for Deformylation Reactions Catalyzed by Cytochrome P-450. *J. Inorg. Biochem.* **1998**, *69*, 241−247.

(13) Wertz, D. L.; Sisemore, M. F.; Selke, M.; Driscoll, J.; Valentine, J. S. Mimicking Cytochrome P-450 2B4 and Aromatase: Aromatization of aSubstrate Analogue by a Peroxo Fe(III) Porphyrin Complex. *J. Am. Chem. Soc.* **1998**, *120*, 5331−5332.

(14) Cho, J.; Sarangi, R.; Kang, H. Y.; Lee, J. Y.; Kubo, M.; Ogura, T.; Solomon, E. I.; Nam, W. Synthesis, Structural, and Spectroscopic Characterization and Reactivities of Mononuclear Cobalt(III)−Peroxo Complexes. *J. Am. Chem. Soc.* **2010**, *132*, 16977−16986.

(15) Kim, B.; Jeong, D.; Ohta, T.; Cho, J. Nucleophilic Reactivity of a Copper(II)-Hydroperoxo Complex. *Commun. Chem.* **2019**, *2*, 81−86.

(16) Shin, B.; Park, Y.; Jeong, D.; Cho, J. Nucleophilic Reactivity of a Mononuclear Cobalt(III)-Bis(*tert*-butylperoxo) Complex. *Chem. Commun.* **2020**, *56*, 9449−9452.

(17) Annaraj, J.; Cho, J.; Lee, Y.-M.; Kim, S. Y.; Latifi, R.; de Visser, S. P.; Nam, W. Structural Characterization and Remarkable Axial Ligand Effect on the Nucleophilic Reactivity of a Nonheme Manganese(III)−Peroxo Complex. *Angew. Chem., Int. Ed.* **2009**, *48*, 4150−4153.

(18) Barman, P.; Upadhyay, P.; Faponle, A. S.; Kumar, J.; Nag, S. S.; Kumar, D.; Sastri, C. V.; de Visser, S. P. Deformylation Reaction by a Nonheme Manganese(III)−Peroxo Complex via Initial Hydrogen-Atom Abstraction. *Angew. Chem., Int. Ed.* **2016**, *55*, 11091−11095.

(19) Cantú Reinhard, F. G.; Barman, P.; Mukherjee, G.; Kumar, J.; Kumar, D.; Kumar, D.; Sastri, C. V.; de Visser, S. P. Keto−Enol Tautomerization Triggers an Electrophilic Aldehyde Deformylation Reaction by a Nonheme Manganese(III)-Peroxo Complex. *J. Am. Chem. Soc.* **2017**, *139*, 18328−18338.

(20) Barman, P.; Cantú Reinhard, F. G.; Bagha, U. K.; Kumar, D.; Sastri, C. V.; de Visser, S. P. Hydrogen by Deuterium Substitution in an Aldehyde Tunes the Regioselectivity by a Nonheme Manganese-(III)−Peroxo Complex. *Angew. Chem., Int. Ed.* **2019**, *58*, 10639−10643.

(21) Pirovano, P.; Magherusan, A. M.; McGlynn, C.; Ure, A.; Lynes, A.; McDonald, A. R. Nucleophilic Reactivity of a Copper(II)−Superoxide Complex. *Angew. Chem., Int. Ed.* **2014**, *53*, 5946−5950.

(22) Bailey, W. D.; Gagnon, N. L.; Elwell, C. E.; Cramblitt, A. C.; Bouchey, C. J.; Tolman, W. B. Revisiting the Synthesis and Nucleophilic Reactivity of an Anionic Copper Superoxide Complex. *Inorg. Chem.* **2019**, *58*, 4706−4711.

(23) Noh, H.; Jeong, D.; Ohta, T.; Ogura, T.; Valentine, J. S.; Cho, J. Distinct Reactivity of a Mononuclear Peroxocobalt(III) Species toward Activation of Nitriles. *J. Am. Chem. Soc.* **2017**, *139*, 10960−10963.

(24) Karlsson, A.; Parales, J. V.; Parales, R. E.; Gibson, D. T.; Eklund, H.; Ramaswamy, S. Crystal Structure of Naphthalene Dioxygenase: Side-on Binding of Dioxygen to Iron. *Science* **2003**, *299*, 1039−1042.

(25) Shin, B.; Sutherlin, K. D.; Ohta, T.; Ogura, T.; Solomon, E. I.; Cho, J. Reactivity of a Cobalt(III)−Hydroperoxo Complex in Electrophilic Reactions. *Inorg. Chem.* **2016**, *55*, 12391−12399.

(26) Gerlich, D. Infrared Spectroscopy of Cold Trapped Molecular Ions Using He-Tagging. *J. Chin. Chem. Soc.* **2018**, *65*, 637−653.

(27) Roithová, J.; Gray, A.; Andris, E.; Jašík, J.; Gerlich, D. Helium Tagging Infrared Photodissociation Spectroscopy of Reactive Ions. *Acc. Chem. Res.* **2016**, *49*, 223−230.

(28) Ugo, R.; Conti, F.; Cenini, S.; Mason, R.; Robertson, G. B. The Addition of Oxygen to Carbonyl Group: The Reactivity of Bistriphyneylphosphineplatinum(0)-Oxygen. *Chem. Commun.* **1968**, *0*, 1498−1499.

(29) Nakazawa, J.; Terada, S.; Yamada, M.; Hikichi, S. Structural Characterization and Oxidation Reactivity of a Nickel(II) Acylperoxo Complex. *J. Am. Chem. Soc.* **2013**, *135*, 6010−6013.

(30) Karlin, K. D.; Nasir, M. S.; Cohen, B. I.; Cruse, R. W.; Kaderli, S.; Zuberbuhler, A. D. Reversible Dioxygen Binding and Aromatic Hydroxylation in O_2-Reactions with Substituted Xylyl Dinuclear Copper(I) Complexes: Syntheses and Low-Temperature Kinetic/Thermodynamic and Spectroscopic Investigations of a Copper

Monooxygenase Model System. *J. Am. Chem. Soc.* **1994**, *116*, 1324−1336.
(31) Liang, H.-C.; Karlin, K. D.; Dyson, R.; Kaderli, S.; Jung, B.; Zuberbuhler, A. D. Dioxygen-Binding Kinetics and Thermodynamics of a Series of Dicopper(I) Complexes with Bis[2-(2-pyridyl)ethyl]-amine Tridendate Chelators Forming Side-On Peroxo-Bridged Dicopper(II) Adducts. *Inorg. Chem.* **2000**, *39*, 5884−5894.
(32) Kripli, B.; Csendes, F. V.; Török, P.; Speier, G.; Kaizer, J. Stoichiometric Aldehyde Deformylation Mediated by Nucleophilic Peroxo-diiron(III) Complex as a Functional Model of Aldehyde Deformylating Oxygenase. *Chem. - Eur. J.* **2019**, *25*, 14290−14294.
(33) Magherusan, A. M.; Kal, S.; Nelis, D. N.; Doyle, L. M.; Farquhar, E. R.; Que, L., Jr; McDonald, A. R. A $Mn^{II}Mn^{III}$-Peroxide Complex Capable of Aldehyde Deformylation. *Angew. Chem., Int. Ed.* **2019**, *58*, 5718−5722.
(34) Andris, E.; Navrátil, R.; Jašík, J.; Sabenya, G.; Costas, M.; Srnec, M.; Roithová, J. Detection of Indistinct Fe−N Stretching Bands in Iron(V) Nitrides by Photodissociation Spectroscopy. *Chem. - Eur. J.* **2018**, *24*, 5078−5081.
(35) Srnec, M.; Navratil, R.; Andris, E.; Jašík, J.; Roithová, J. Experimentally Calibrated Analysis of the Electronic Structure of CuO^+: Implications for Reactivity. *Angew. Chem., Int. Ed.* **2018**, *57*, 17053−17057.
(36) Andris, E.; Navratil, R.; Jasik, J.; Srnec, M.; Rodriguez, M.; Costas, M.; Roithova, J. M-O Bonding Beyond the Oxo Wall: Spectroscopy and Reactivity of Cobalt(III)-Oxyl and Cobalt(III)-Oxo Complexes. *Angew. Chem., Int. Ed.* **2019**, *58*, 9619−9624.
(37) Rice, D. B.; Massie, A. A.; Jackson, T. A. Experimental and Multireference ab Initio Investigations of Hydrogen-Atom-Transfer Reactivity of a Mononuclear Mn^{IV}-oxo Complex. *Inorg. Chem.* **2019**, *58*, 13902−13916.

https://doi.org/10.1021/jacsau.1c00166
JACS Au 2021, 1, 1594−1600